

The 1994-95 apparition of Mars observed from Pic-du-Midi

Stéphane Erard

Institut d'Astrophysique Spatiale, bât.121, 91405 Orsay campus, France.
CNRS, Université Paris-11.

Contact address : S. Erard,
Erard@ias.fr
tel : 33 1 69 85 86 41
fax : 33 1 69 85 86 75

33 Pages
10 Figures (13 sheets)
4 Tables

Abstract

The 1995 apparition of Mars was monitored with the Pic-du-Midi 1-m telescope from October 1994 to March 1995. Several thousand images were acquired with a CCD camera through various filters ranging from 0.4 to 1.05 μm . These images complete HST observations of the same apparition with a spatial resolution reduced by a factor of ~ 4 , but with a better time resolution. Low resolution spectra were also acquired through a set of interferential filters at opposition, providing indications of mineralogical composition of surface materials. The only significant surface variations during the period are observed in the Cerberus area, which brightened at the end of winter. The whole apparition was very cloudy. The north Polar Hood dissipated in early December ($L_S \sim 25^\circ$). Migration of polar clouds to the equator is observed between January 31 and February 6 ($L_S \sim 50^\circ$ - 55°). Then an Encircling Cloud Belt obscured most of the surface from February 22 to 24 at least ($L_S \sim 62^\circ$). The north polar cap regression is similar to that observed by Mariner 9, although several internal rifts developed during early spring, in particular the dark Lowell band and Rima Tenuis. A standstill is observed in the polar cap regression curve from $L_S = 55^\circ$ to 70° at latitude $\sim 70^\circ$, at least in the 135 - 300° longitude range. The very strong spectral feature at 0.95 μm reported from HST observations of Olympia Planitia in July 1995 is not observed in the Pic-du-Midi images. The intermediate-dark region of Propontis I exhibits ferric absorption features consistent with high concentrations of crystalline hematite or other dark ferric materials.

Introduction

This survey of Mars during the 1994-95 apparition was originally related to the preparation of the Russian mission Mars-96. It was specifically intended to optimize the observation program of the imaging spectrometer OMEGA. One of the main interests was to assess the possibilities to observe the north polar cap, since high northern latitudes were accessible only at the very beginning of the mission, due to orbital constraints. This work was postponed after the loss of the spacecraft at launch. However, the upcoming Mars exploration and sample return program calls for an increase of the observational records, to clarify the context for future missions. Some of the foreseen missions will give unprecedented opportunities to study the polar regions from high inclination orbits (*eg.* Mars Surveyor 2003 and 2005, Mars Express). Surface stations (*eg.* Beagle II, Netlander, MSR), landed either at high or low latitudes, will include payloads dedicated to the study of the Martian climate and would also greatly benefit from continuous observation programs.

Earth-based observation remains the only practicable way to perform continuous surveys of the planets; a very good planetary site with limited demand for observational time like the 1-meter telescope at Pic-du-Midi provides the optimal opportunity to monitor planetary activity, including atmospheric phenomena, surface variations and polar caps evolution. So far, spacecraft observations are conversely limited to very narrow periods, and concern only few Martian years.

HST observations of Mars, although yielding a much better spatial resolution (*eg.* James *et al.* 1996a, James *et al.* 1996b), are limited to very few sessions due to observational schedules and solar pointing constraints. In a threefold approach where spacecraft yield exceptionally detailed but exceptionally rare data, and space-borne observatories provide high resolution at limited viewing geometry on a year-to-year basis, ground-based observation is still the only method to monitor quick processes like polar recession, atmospheric activity, and surface changes along a complete Martian apparition.

Seasonal variations of the Martian polar caps are a major factor controlling atmospheric phenomena and surface changes, and many of those appear to be directly coupled to the strong currents of matter between the two polar caps. It has long been observed for instance that atmospheric clouds and hazes are more frequent at low latitude when the spring polar cap waxes rapidly, so that large quantities of H₂O and CO₂ are released in the atmosphere. Records of the polar caps recession exist for more than a century (*eg.*, Antoniadi 1930, Capen and Capen 1970, Dollfus 1973, Iwasaki and Saito 1979, Iwasaki and Saito 1982 and references therein). Orbital observations of the north polar regions have been performed by Mariner 9 in 1972 (Soderblom *et al.* 1973) and Viking in 1977-78 (*eg.*, James 1979) and 1979-80 (*eg.*, James 1982, Christensen and Zurek 1984). The Hubble Space Telescope also performed observations during the last four oppositions, from 1990 to 1997 (Cantor *et al.* 1998, James *et al.* 1996a, James *et al.* 1996b, James *et al.* 1994, Wolff *et al.* 1997). The recession of the north polar cap is less documented than the southern one, because the north pole is tilted toward the Earth only during aphelic oppositions, when the planetary distance is larger and the disk is smaller. However, both polar regions are known to exhibit similar behavior during their respective early-spring periods. The 1995 apparition of Mars was an aphelic one and consequently took place during the northern hemisphere spring, permitting to study the north polar cap recession. The tilt was larger than during the previous two oppositions, so this was the first good opportunity to observe the northern cap ever since CCD technology existed.

Background

During winter ($L_S=340^\circ-10^\circ$) the north polar cap is concealed by gray, opaque condensates known as the Polar Hood. Around vernal equinox, the Polar Hood dissipates and the polar cap appears with its maximum extension, down to 60° N; at this time it exhibits a smooth and uniform border. Although some observations suggest that the polar cap reaches full extension only in late winter (Akabane *et al.* 1993, Iwasaki and Saito 1979), it starts receding as soon as it emerges from the Polar Hood. Recession pauses at about 66° latitude between $L_S\sim 20^\circ$ and 45° with important annual variations (*eg.*, James 1979), then resumes at a more rapid rate after $L_S\sim 55^\circ$. The edge of the cap then appears uneven, due to frost deposits and to persistent H₂O and CO₂ hazes, as seen in Viking data (Christensen and Zurek 1984). In the northern hemisphere, the recession is often slowed down at the end of spring, and the cap may even grow again as the planet approaches aphelion (“aphelic chill” around $L_S=60-75^\circ$, Capen and Capen 1970). By summer the recession is almost complete, and three detached outliers usually remain behind the cap’s edge, at positions that can vary from one opposition to the other. A cap remnant persists through summer beyond 80° in latitude. A rift crossing the cap has been reported at the beginning of the century, and again during the 80’s, during summer ($L_S\approx 70^\circ$); this feature, called Rima Tenuis by Schiaparelli, is not confirmed however and is located where HST observed a system of dust streaks during the 1995 opposition (Wolff *et al.* 1997).

Unlike the south one, the north polar cap always remains nearly centered at the pole. Comparison of historical observations shows that both the rate of recession and the size of the permanent polar cap are rather constant from one opposition to the other (*eg.*, Iwasaki and Saito 1979, Dollfus 1973, and references therein). A “normal” recession has been defined by Fischbacher *et al.* 1969 for each hemisphere, by comparing a number of oppositions from 1882 to 1969. More recent comparisons indicate however that the north polar recession started later but was more rapid during the 80’s than during the 60’s, and that the cap remnant was significantly smaller (*eg.*, Parker and Beish 1995).

Viking observations showed that the permanent north polar cap is composed mainly of water ice, unlike its southern counterpart that is made up of CO₂ (Kieffer *et al.* 1976, Farmer *et al.*

1976). This discrepancy has strong repercussions on the Martian climate, since summer temperatures at the north pole can be much higher than in the south and may result in relatively large release of water vapor. During spring and early summer water vapor is also released by the regolith at higher latitudes (Haberle and Jakosky 1990). Clouds are often observed moving away from the pole in this season and form large systems at lower latitudes, with concentrations on the volcanoes and above Valles Marineris; a sharp increase in circumpolar clouds has been observed when recession resumes at $L_s \sim 50^\circ$ (James *et al.* 1987). Lower temperatures normally result in lower condensation level and larger atmospheric opacity. Delays in the recession have been correlated to unusual amounts of atmospheric dust in the polar regions: heat absorption by dust may be sufficient to influence polar temperatures, and to trigger frost deposition (James 1979). In some instances this can result in reduced water transport and reduced cloud formation at lower latitudes. Conversely, the presence of numerous clouds is often regarded as a precursor sign of large dust storms (*eg.*, Martin and Zurek 1993). The interactions between water, CO_2 , and dust cycles are very complex however, and there is no clear correlation between cloudiness, polar recession rates, and dust concentration in the observational records (see reviews in James *et al.* 1992, Forget 1997).

Data acquisition and reduction

The images used in this work were acquired from October 1st, 1994 to March 13th, 1995 with the Pic-du-Midi 1-meter telescope by a team composed of Jan Rosenqvist, Jean Lecacheux, François Colas, Pierre Drossart, and myself (Station de planétologie des Pyrénées). This period bracketed opposition with phase angles in the range $38^\circ - 3.2^\circ - 22^\circ$ (see Table 1), and corresponded to spring on Mars' northern hemisphere ($L_s = 355^\circ$ to 71°). In this season Mars is close to aphelion, so it appears very small as seen from the Earth. Conversely elevation is maximum at this time in the northern hemisphere; it reached 64° at Pic-du-Midi at opposition (February 12th) and observing conditions were then optimum. The best spatial resolution was achieved around opposition when the angular size of Mars was $\sim 14''$ only, corresponding to 130

CCD pixels across the disk. Seeing was estimated to 0.3'' during the good periods (usual at Pic-du-Midi), hence at opposition all pixels are resolved; this corresponds to a resolution better than 150 km at the disk center. At this moment, the central meridian was in the Elysium hemisphere during most of the night.

All observations were performed using a Barlow lens, yielding a focal distance of 43 m. The detector used during most of this period was a Thompson 384 × 288 CCD camera and the signal was digitized on 12 bits. The camera was cooled down and maintained at -103°C. At this temperature, dark current variations are on the order of 0.9 DN. A set of large band and interferential filters was used between 0.4 and 1.05 μm. The typical signal to noise ratio in I filter is about 300, with integration times ranging from 0.1 s (I filter) to 3 s (B filter). Interferential filters have a much narrower bandwidth and required longer integration times, specially at short and long wavelengths where the CCD response is low (up to 30 s at 0.40, 0.98, and 1.02 μm). Flat fields were acquired for each night and each filter. Reference stars were observed during some of the nights only, so that images are not calibrated in flux in the present study. Image quality was controlled in real time, and only images with good contrast and seeing were recorded. Several hundreds of images were acquired during good observation nights.

The filters used in this study are mainly broad-band B, V, and I filters, plus R and RG 695 filters when I images were not available or were of poor quality (see Table 2). Interferential filters were used near opposition to get low-resolution spectra of surface units, as detailed below. Clouds, hazes and the polar cap appear very bright in B filter, while the surface is dark with minimum contrast. V filter provides average surface contrast and maximum contrast between the cap and soils. I filter provides maximum surface contrast, but similar reflectance for bright terrains and the polar cap, and dust clouds appear very bright. Reduction first consists in the selection of images of outstanding quality. The average value of the dark sky is removed from individual images in order to subtract the dark current and the scattered light; this dark signal is computed using only columns of the CCD that are entirely in the dark sky, so as to avoid frame transfer contamination. Images are then flat-fielded using average exposures of the sky. Since the signal to noise ratio of individual images is already very high, the images are not averaged so as to preserve

spatial resolution. Modest unsharp masking is applied to the images shown in Fig. 1 and 7 to enhance local contrast.

In order to retrieve geographical coordinates and to mosaic maps, image orientation, disk center coordinates, and disk radius must be known precisely. Image orientation depends on the relative attitude of Mars and the Earth, and on the orientation of the camera in the focal plane. Photometric coordinates and illumination angles are interpolated from ephemerids computed with a time step of 10 min. The camera angle changed every time the camera was removed for maintenance, and was not systematically calibrated. In the absence of angular calibration, this angle is retrieved by comparing images acquired at intervals of several hours: images with similar seeing are projected on a cylindrical coordinates system, assuming a value for the camera angle. The camera angle is then adjusted to provide maximum correlation between the projected images. Only the central part of the disk is used in this procedure (emergence $\leq 50^\circ$), and a global Minnaert correction is applied to the disk in order to correct low frequency variations. Images in V filter are used preferentially to determine this angle, because they were found to be less sensitive to limb effects related to clouds and dust. Once the image orientation is known, the sub-terrestrial point (disk center) and the disk contour are located on the images by fitting a circle to the illuminated limb, where the intensity gradient is steeper. Determination of the limb position relies on a threshold level that is controlled interactively for every night and filter.

Cylindrical maps (Fig. 2 and 8) are built from selected images in I and B filters, showing respectively surface features and atmospheric formations. Two or three images are selected for each observation night, in order to get the maximum longitudinal coverage. Images are first corrected with a Minnaert function, the exponent of which is fit for each couple of images (see below). Images are then reprojected assuming that the disk is circular. Only the central part of the disk ($e, i < 60^\circ$) is used in these maps so as to minimize departures from the average Minnaert's function. Since reference stars were not available for each night, individual images cannot be scaled in absolute reflectance and do not compare directly. Instead, consecutive images are matched using the regression line in the region of overlap. Finally, the overlap regions in the mosaic are merged smoothly to improve continuity, and therefore albedo differences in Fig. 2 and

8 are only indicative. Following the method described by de Grenier and Pinet 1995, I have spanned the range from 0.5 to 0.8 for the Minnaert exponent, and looked for the value that minimizes the residual dispersion in the overlap region. The Minnaert exponent derived this way is adapted to each filter and phase angle, but it is an average on a large area that varies with the attitude of Mars and the albedo pattern exposed at a given time (the polar regions are always excluded from the overlap region). The values retrieved here are usually $k = 0.65-0.70$ in I and $k \approx 0.6$ in B (Tables 3 and 4), which agrees with most previous observations of the bright terrains (*eg.* Binder and Jones 1972, de Grenier and Pinet 1995). In regions also used by de Grenier and Pinet (observed in 1988), the exponents computed in the nearest filter fit within the error bar with the exception of February 22 in B filter, when limb darkening is controlled by the large atmospheric scattering. The largest discontinuities in the present mosaics are on the order of 15%. They are found on the border of the polar cap, and are related to a faster limb darkening rate on the cap than on the soils or rocks.

Polar maps are built from selected images in I, V, and B filters (Fig. 4). The contrast between soils and the polar cap is maximum in the V filter, but these images are found more sensitive to photometric effects than I images, and hence are generally more difficult to mosaic. However, I images are more sensitive to dust in the atmosphere. B images are useful to identify possible clouds or mists. In some instances when no I filter images were available, I have used images acquired through the RG 695 filter instead (similar to I, slightly wider). A Minnaert correction is again applied to individual images, with an exponent determined for each night and filter, regardless of terrain albedo and composition; consequently, the exponents used in Fig. 4 are trades-off between values adapted to the soils and cap, and have little physical meaning. The exponents determined for these maps are on the order of 0.75 ± 0.05 in V filter and 0.85 ± 0.05 in I filter, larger than those used for cylindrical maps because of much stronger limb darkening rate on the polar cap. Images are then transformed in geographical coordinates using a Lambert equal area projection centered at the north pole down to 50° latitude, assuming that the Martian disk is circular. Finally, images are scaled relative to one another and composited. In the maps presented Fig. 4, I've tried to cover all latitudes up to the pole itself so as to get a view of the cap as complete as possible; regions observed under incidence or emergence angles larger than 70° ,

where the Minnaert correction yields spurious results, are always clipped. The Minnaert model is however approaching its limits for such large angles, which results in a rather large residual dispersion in the fits (on the order of 15-20%), with maximum residuals near the pole. Other remnant discontinuities are present on dark terrains, because the average exponents are too high to fit their photometric behavior. The maps presented here correspond to phase angles ranging up to 34° , whereas the Minnaert model is valid up to $\sim 30^\circ$ phase angles on smooth surfaces. However, comparisons of various photometric models suggest that when considering surfaces with small-scale roughness typical of terrestrial planets, Minnaert functions remain a good approximation of more physical models for phase angles as high as 60° (eg. McEwen 1991).

For both types of maps, the accuracy of the projection is limited by the uncertainty on the camera angle (less than 1°), the polar flattening of the Martian disk (0.7 pixels at opposition), and the determination of the disk edge (about 1.5 pixels). Uncertainties combine to yield a maximum projection error of $\sim 1.5^\circ$ in longitude and latitude at the disk center, and $\sim 5^\circ$ in latitude at 80° latitude. The largest source of error appears related to the determination of the disk edge. In general this error is larger than the dispersion between measurements, and is therefore probably over-estimated.

Surface features and spectra

Surface markings

Most of the variability observed during this period is related to atmospheric activity and to recession of the north polar cap. As discussed below the atmosphere was particularly cloudy during most of the apparition, with several short episodes of large atmospheric opacity. An incredible wealth of detail is observed in the dark regions throughout the apparition (Fig. 1). Conversely, bright areas exhibit only smooth and regular variations. Figure 2 displays a map of surface features spanning all longitudes at the time of opposition. This map is a mosaic of 3 cylindrical maps computed as described in the previous section, using images acquired through the

I filter on January 31st, February 6th, and February 22nd. Surface markings remained fairly constant during the period of observation, with the exception of Cerberus, a dark region southeast of Elysium Mons. This feature has remained very dark from the beginning of the century to the early 60's, then experienced large variations in albedo, and weakened during the 80's. It appears very pale in the 1995 HST images acquired on February 25th (James *et al.* 1996a), but has been reported to be darker earlier in the apparition, and to darken again after march 1995 (Troiani *et al.* 1996). Our images confirm that Cerberus was uniformly dark in mid-November ($L_s = 20^\circ$) as it appears on the Viking maps, then reduced to three discrete dark spots from January 31st to March 13th at least (Fig. 3. The contrast with neighboring regions is $\sim 8\%$ in the dark spots and 2% in the central part on reduced I images). This period includes nights of minimum atmospheric opacity, hence the evolution observed is not due to brightening by clouds; nearby dark regions in this hemisphere exhibit no obvious change during the apparition, so the variations in Cerberus are probably related to seasonal migration of bright materials from the adjacent bright areas, possibly under the influence of the strong winds from the north polar regions. All this area has suffered substantial changes in the past 10 years; one of the most striking difference with the 1988 opposition for instance is the darkening of the northernmost part of Terra Cimmeria at longitude 220° and latitude -10° (in the vicinity of the Herschel crater), where two dark elongated features were barely visible in 1988 (*eg.* Pinet and Chevrel 1990, Lecacheux *et al.* 1991) and are conversely very prominent during all the 1995 apparition, with a contrast reaching 25% relative to neighboring regions.

Another interesting surface feature is the dark collar developing inside the polar cap between latitudes 78° and 85° (Fig. 1 and 4). This feature, known as the "Lowell band", corresponds to surface markings that can be observed later in the summer when these regions are completely free of ice. It was reported *eg.* by Dollfus 1973 at the same location during the oppositions of 1946 and 1952, when the ring clearly corresponded to a gap between the central part of the cap and large icy deposits or frozen areas further from the pole. The Lowell band is thus a dark region where the ice probably sublimates more rapidly than on the border, due to the lower thermal inertia of the underlying material, while ice or frost remain longer in bright areas at lower latitude. In the Pic-du-Midi images, the dark ring is very prominent in I and R filters. It is

observed also in V filter and in some instances in B; V observations are in general more sensitive to changing photometric effects induced by the atmosphere. Although very narrow and subdued, the dark collar is present as early as November 20 ($L_S = 20^\circ$), then becomes distinctly visible in both I and B filters on December 16 ($L_S = 34^\circ$). It is apparent until the end of our observation period on March 13, but maximum contrast is reached just before opposition, from January 31 to February 9 (~10% in I images, and 5% in B). This variation in contrast can be related either to the evolution of the polar cap or to changing observation conditions (disk size, seeing, opacity...). In HST images acquired in summer ($L_S = 135^\circ$), the dark band distinctly appears as a soil unit encircling the permanent polar cap down to 75° latitude, with cap outliers remaining at lower latitudes. The feature is not symmetric, the ring being larger and darker at longitudes 250° - 320° and 120° - 170° . The first area corresponds to a zone of barchan dunes. The second one corresponds to the very dark Olympia Planitia that has been interpreted from Viking images as a field of transverse dunes made of basaltic sands (Tsoar *et al.* 1979). This is the darkest part of the collar, and apparently the first region where the ice melts completely to reveal the underlying materials; it corresponds very closely to the area of lowest thermal inertia derived from IRTM measurements (Paige *et al.* 1994).

Surface spectra

HST performed multi-filter observations of Mars several month later, at $L_S = 122$ - 145° . These observations have been discussed by Bell *et al.* 1997a and Bell *et al.* 1997b. In the former paper, the authors discuss an absorption of 25-30% centered around $0.95 \mu\text{m}$ in the Lowell band, *ie.* one of the strongest spectral features ever observed on Mars in the near-infrared. The feature was tentatively ascribed to low-Ca pyroxenes, and its unusual depth to coarse grain materials. However, spectral photometric effects (*eg.*, variations of Minnaert exponent with wavelength) are not accounted for in the HST data, and could also contribute to deepen the band in regions observed under larger emergence and incidence angles. Spectral photometric effects have been demonstrated from a detailed study of narrow band filters observations of the 1988 opposition (de Grenier and Pinet 1995). The observations used by de Grenier and Pinet were acquired from the

2m telescope at Pic-du-Midi using a set of near-infrared interferential filters selected to study surface mineralogy (see Pinet and Chevrel 1990).

We also used a variety of interferential filters near opposition, when the disk size was large enough to allow reasonable integration times. This set includes some of Pinet and Chevrel's filters, and is completed to provide a better spectral coverage in the visible (see Table 2). Direct ratios of disk images are not very informative, because misregistration artifacts due to the planet rotation can be on the same order of magnitude as the expected spectral features (filter sequences are typically acquired within 30 min). To avoid this problem, images are reprojected on a common latitude/longitude grid prior to being ratioed; this method also makes it possible to compare images largely separated in time. I have built such an image cube from all the interferential filters used on February 6th. The best images are selected and reprojected on polar-Lambert maps ranging from the equator to the pole, using a Minnaert correction optimized for these particular images. The Minnaert exponents are equal to 0.85 above 0.73 μm , to 0.75 at 0.514 μm and 0.583 μm , and to 0.60 at 0.40 μm . These values are adapted to the soils, not to the polar cap that has a more Lambertian behavior (Minnaert exponent close to 1). The exponents derived here agree with previous observations of bright regions (*eg.*, de Grenier and Pinet 1995), except at 0.4 μm where the only previous photometric study yielded an exponent of 1 (McCord and Westphal 1971); this discrepancy is consistent with a particularly clear atmosphere on February 6th however, since surface features, including the Lowell band, were distinctly observed through the B filter that night (~15-20% contrast between bright and dark areas). Finally, the images are scaled to a spectrum of a typical mid-latitude bright region from Erard and Calvin 1997. This reference spectrum is a composite of telescopic visible data from Bell *et al.* 1990 measured on Ascraeus Mons (below 0.77 μm), and space-borne infrared data from Phobos-2/ISM measured on Ophir Planum (58°W and 5°S). Both spectra were acquired under similarly low opacity at near normal geometry, and therefore are comparable to the Minnaert corrected images. Consequently, all images are scaled so that the average value in Arabia Terra is equal to that of the reference spectrum convolved with the filters response. The image cube is then composited from the scaled images. In this procedure, the main source of uncertainty is probably not related to the difference in the reference areas (that were selected for their large similarity and uniformity), but rather to

possible differences in the magnitude of aerosols scattering in the Martian atmosphere during observations. A systematic calibration error could therefore produce an incorrect spectral slope, but would not result in spurious absorptions. The uncertainty related to the photometric correction is estimated by comparison with data corrected using a smaller exponent. The uncertainty on the Minnaert exponent is estimated to 0.05 on bright areas, and to 0.25 on dark areas (at all wavelengths). The main effect of a smaller exponent is to change the average level of the spectra by up to 15%. When considering spectra normalized in the NIR range, the maximum uncertainty is limited to 3% above 0.73 μm (0.4% in bright areas), and is usually smaller than 20% in the visible (some % in bright areas). This maximum uncertainty is represented by the error bars on Fig. 6. Although the possible error on the spectral slope in the visible range is rather large, the absorption bands at 0.90-0.98 μm are several times deeper than the uncertainty in this range. Therefore, the correction does not seriously affect the absorption bands in the NIR range. Examples of spectral ratios are shown in Fig. 5. The 0.73 / 0.58 μm ratio represents the spectral slope in the visible, and increases with albedo on ice-free terrains (signal to noise is ~ 250 , uncertainty due to the Minnaert correction is 4%, mostly at low spatial frequencies). The second map is a measurement of iron absorption, computed as the ratio of the intensity at 0.90 μm to an estimate of the continuum at this wavelength ($I(0.73)^{d\lambda} * I(0.98)^{(1-d\lambda)}$ where $d\lambda = 0.32$ accounts for the spectral distance between filters, see *eg.* Erard *et al.* 1991). The signal to noise ratio is ~ 180 , the uncertainty due to the Minnaert correction is 7%, with the largest values on Syrtis Major. This spectral parameter is mostly related to pyroxenes and is found to be globally correlated with albedo. In Vastitas Borealis (the circular dark region at latitude 50°), the gradient of this ratio towards the pole is probably related to the areal proportion of ice at subpixel level, or to ice clouds.

Spectra of several regions of interest shown in Fig. 6 are averaged over 20-40 pixel areas, far from albedo boundaries. The footprints of the spectra are showed on Fig. 5a, superimposed on the ratio of intensities at 0.78 and 0.58 μm . The statistical dispersion in each area, which includes noise, inhomogeneities, and possible registration problems, is several times smaller than the symbol size in Fig. 6 (less than 0.4%). Spectra are extracted where artifacts due to pixels resampling are minimum. The overall dynamic range in the image cube is consistent with that of

the composite spectra from Erard and Calvin 1997. Spectra themselves are similar to those reconstructed from HST observations during the same opposition (Bell *et al.* 1997a), except at 0.4 μm where HST spectra of the cap are significantly brighter. This difference is consistent with intense Rayleigh scattering in the atmosphere in July 1995 as opposed to a very clear atmosphere on February 6th. Alternatively, it could result from an error in the Minnaert exponent used here.

The polar cap spectrum has a strong absorption near 0.98 μm due to H₂O ice, either as frost on the cap surface or as ice clouds in the atmosphere; its very steep spectral slope in the visible demonstrates that the cap is fairly red, which contradicts the assumption usually made when scaling color composite images of Mars. This has been previously noticed for the residual north polar cap by Bell *et al.* 1997a from images calibrated with the HST pipeline. In ice-free regions, the 0.98 μm absorption due to silicates is shallower and always wider than the water-ice feature in the cap spectra, and also affects the level at 0.90 μm . In bright regions such as Elysium or Arabia, reflectance is always lower at 0.90 μm than at 0.98 μm , indicating a band centered at shorter wavelength, and likely related to iron oxides. In dark regions such as Syrtis Major or the dark part of Utopia Planitia, maximum absorption occurs at 0.98 μm and indicates an absorption centered between 0.90 and 0.98 μm , related to mafic minerals. The spectrum of Olympia Planitia in Fig. 6 is extracted from the dark Lowell band. Although very bright, it is $\sim 10\%$ darker than its surrounding and has spectral features similar to those of the darkest part of Utopia. The “excess” intensity relative to Utopia can be due to the Minnaert correction (adapted to bright soils, and probably exaggerated for dark materials), to subpixel ice deposits, or to spatial blurring. In this area the measured absorption has a depth of 5-7% only relative to bright areas, slightly smaller than the 8-10% absorption measured in low-latitudes dark regions (Syrtis Major or Utopia Planitia), so I do not see evidence for the very large (25-30%) absorption apparent in HST data at 0.95 μm . Yet our observations were performed when the dark collar was still surrounded by ice deposits, while HST images were acquired 5 month later with a spatial resolution about three times better. If subpixel deposits or spatial blurring are responsible for the relatively high reflectance of the dark collar in Pic-du-Midi spectra, they might also account for the difference in band depth with HST observations. In addition, spectral coverages do not compare very well and would favor deeper absorptions in HST data if the band is centered at $\sim 0.95 \mu\text{m}$ rather than

0.98 μm (*ie.*, related to low-Ca orthopyroxenes as proposed by Bell *et al.* 1997a, rather than high-Ca clinopyroxenes). Spectral photometric effects (related to incidence and emergence angles) mentioned above as a possible explanation for the deep HST feature do not explain the difference, because the Minnaert exponent fit on our images is constant above 0.73 μm , and because the rotation of the planet is small between images in different filters. However, the data are acquired under very different phase angles (36.8° for HST, 5.7° for the present spectra). Spectral contrast often increases with larger phase angles, so that the difference between HST and telescopic spectra in regions such as Olympia can still be due to, or be enhanced by, photometric effects.

The spectra are interesting in two other respects. First, the ratio of images at 0.98 and 1.02 μm is rather low in dark areas (0.94 to 0.98), suggesting that olivine is not a major component of polar dark sands or any other region in the northern hemisphere between longitudes 180° and 320° at a spatial scale of ~ 200 km. This is consistent with recent near-infrared observations at higher spatial resolution (*eg.*, Erard *et al.* 1991, Bell *et al.* 1997b). Second, the dark spot known as Propontis I (W of Arcadia Planitia at 35° N latitude) has a particular spectral behavior, and exhibits the deepest 0.90 absorption in the image cube ($>7\%$), with no indication of absorption at 0.98 μm . Bands centered at such short wavelengths are often indicative of ferric absorptions in iron oxides, and the large band depth suggests a relatively well-crystallized material. Associations of low to intermediate albedo and ferric absorptions are not common on Mars, but have been reported in particular in eastern Syrtis Major (*eg.*, Erard *et al.* 1991, Bell 1992), southwest Claritas Fossae, south Daedalia Planum and Sirenum Fossae (Martin *et al.* 1996), Deucalionis Regio (Merényi *et al.* 1996), and in Sinus Meridiani in the north (Murchie *et al.* 1996) and south (Christensen *et al.* 2000, Lane *et al.* 1999). These terrains were interpreted either as mixtures including crystalline hematite, or as coverages of dark ferrous materials by altered ferric dust. In the latter case however, ferrous absorptions are still visible at 0.98 μm . Because of the complete lack of absorption at 0.98 μm in the present spectra of Propontis I, the presence of crystalline hematite is favored.

Atmospheric activity

Atmospheric opacity cannot be measured from the images, because standard stars are not available for each night and the images cannot be calibrated in intensity. Cloud formations are nonetheless clearly visible on B images. Atmospheric activity is therefore monitored on images and cylindrical maps in B filter (Fig. 7 and 8). Such images are available for 15 nights, and maps are computed as described in section “Data acquisition”. Only the central part of the disk is used in the maps, so that only local clouds (as opposed to limb clouds) are present in these pictures. Limb clouds are monitored on the images themselves. As noted by other observers (*eg.*, Parker and Beish 1995) the atmosphere was rather cloudy during the whole apparition, with at least two clearings observed on December 16 and February 6 (Fig. 7 and 8). A continuous equatorial cloud band developed on February 22 (also observed in HST images of February 24). Such cloudy situations have been considered precursor signs for large dust storms (Martin and Zurek 1993); however, only small local storms were observed during this apparition and the following. No major dust cloud is actually apparent in our images, where only local brightenings are observed in I and V filter, in particular on February 5 in Amazonis (SW of Olympus Mons).

On October 2 ($L_S = 356^\circ$), the polar hood is clearly apparent. Orographic clouds are present on Elysium and surface contrast is reduced in B filter. On November 20 ($L_S = 20^\circ$) the polar hood has largely dissipated and the cap is apparent, although still cloudy. No surface markings are seen through the cap (the Lowell band is already visible on the HST R image of November 18). Local clouds are observed in Amazonis and Elysium, a marked nebulosity is visible over Isidis and Lybia, and fogs are present in the Hellas basin. On December 16 ($L_S = 32^\circ$) the atmosphere is very clear and transparent, but intense continuous hazes are present at the morning limb, and fogs are still observed in Hellas (Fig. 7a). An important nebulosity is also observed on the border of the cap, north of Acidalia. Last, a dark structure is observed inside the cap at longitude $\sim 330^\circ$, that corresponds in position to Rima Tenuis. This feature was observed from the end of December by many observers, and possibly as soon as December 2 from Europe (see Troiani *et al.* 1996).

On January 31 ($L_S = 53^\circ$) the atmosphere is still rather transparent, with high surface contrast in B images (Fig 8a). Bright orographic clouds are present from this moment until the end of our observation period over Elysium, Olympus, and the Tharsis Montes. On February 3 and 5, nebulosity seems more pronounced and surface details are no longer apparent in B filter at low latitudes. Orographic clouds are fully developed, clouds also cover Arcadia and Noctis Labyrinthus, and limb clouds are present. However, the dark Lowell band becomes apparent in B, which suggests that polar clouds dissipate, so that the evolution during this week seems to correspond to a migration of clouds from polar latitudes to the equator. On February 6, the whole atmosphere is again very transparent in B filter, with only localized clouds on the volcanoes and in Hellas, and a bright limb cloud over Syrtis (Fig. 7b). On February 9 clouds are less distinct, but are present on Tharsis, Arcadia/Tempe and Chryse/Xanthe. Limb clouds are observed on the cap border, and dissipate in the morning.

On February 22 ($L_S = 62^\circ$) B images are very bright and surface details are barely visible (Fig. 7c). Continuous clouds girdle the low latitudes between $\sim 10^\circ$ and $\sim 30^\circ$ N, with maximum opacity over Tharsis and Amazonis; on Pavonis and Ascraeus, clouds are as bright, or even brighter, than the polar cap (versus 75% intensity on February 6, Fig. 7c and 8b). This Equatorial Cloud Belt (ECB) is still present on HST images of February 24. The development of this cloud belt has been considered the most salient feature of the apparition by James *et al.* 1996a, who estimated its total water content to 1 μm from HST images. According to James *et al.* 1996a, the development of such a belt in this season is consistent with atmospheric models and increased water vapor condensation related to reduced sunshine near aphelion, specially in the absence of dust (aphelion is at $L_S = 71^\circ$, March 14). ECB are very rare in the observational records, although another one has been observed during the 1992-93 apparition. However this rarity can be a bias related to observational technics (see discussion in Troiani *et al.* 1996). By early March, situation has partly returned to normal: the cloud belt persists, but contrast increases in B, and orographic clouds in Tharsis appear again as individual features.

Seasonal north polar cap

The most obvious structure in the polar cap during the 1995 apparition is the Lowell band discussed in section “Surface features”. Ice deposits or frosts remain southward of the ring until February 6. On February 22, regions between $\sim 20^\circ$ and $\sim 100^\circ$ longitude are mostly free from ice deposits (Fig. 1 and 4).

Other dark features are apparent within the cap on two occasions. First, the Rima Tenuis feature is observed at $\sim 330^\circ$ longitude on December 16, as described above. Second, from February 3 to 6 a dark structure is again visible observed the cap, this time at $\sim 155^\circ$ longitude. On February 5 and 6, this feature is fully apparent in both I and B filters (Fig. 1a at $L_S = 55.2^\circ$, and Fig. 7b). It is not observed on January 31, and no longer distinct on February 9. It could correspond to the other part of Rima Tenuis, which was observed as a continuous rift in the cap at this time, although apparently at a slightly different position (see Troiani *et al.* 1996, Warell 1996).

The recession of the north polar cap is illustrated on the polar projections in Fig. 4. The cap is still covered by the polar hood at $L_S = 356^\circ$. At $L_S = 20^\circ$, it has become very apparent and extends down to 60° in latitude. The characteristic “polygonal shape” is observed in late January, as noticed by James *et al.* 1996a. Indeed, the map of February 6 ($L_S = 55.2^\circ$) compares very well with Fig. 5 from James *et al.* 1996a, obtained with HST on February 24 ($L_S = 63.5^\circ$).

I have measured the limits of the polar cap essentially from cylindrical projections of I images. The images are reduced and corrected from limb darkening assuming Lambertian behavior (adapted to the polar cap), then images are resampled on a cylindrical grid as described in section “Data acquisition”. Meridian profiles are extracted from the cylindrical maps every 10° longitude in the range $\pm 40^\circ$ from the subterrestrial longitude (this range corresponds to a $\sim 50\%$ increase of the standard error on the polar cap limit). The cap limits are then extracted automatically from each profile. The criterion used to locate the cap border is that defined by Cantor *et al.* 1998 from modeling of HST images: the limit is taken where the contrast between the peak cap intensity and the surrounding terrains is reduced by 55%. Automatic measurements are controlled interactively, and checked using R or V maps and unprojected I images. Although I images are generally of

better quality, they exhibit reduced contrast between bright regions and the polar cap, and they are sensitive to dust storms or clouds at high latitudes. Measurements are performed on R or RG 695 images whenever I images are not available or yield spurious results. Two problems are found with this method: first, the maximum intensity is not always on the visible part of the disk, depending on the tilt of the planet; second, the Minnaert correction can lead to biased measurements when the cap limit is located near the disk edge, and for high phase angles. For this particular opposition, these problems are found to be more important at low L_S .

Cap edge measurements are shown on Fig. 9, and longitudinal variations are illustrated in Fig. 10. In general, the Pic-du-Midi data agree with measurements performed on HST images (Cantor *et al.* 1998), and they provide extra data points at intermediate dates. As mentioned by James *et al.* 1996a on the basis of HST images, the 1995 recession curve is generally similar to that observed by Mariner 9 in 1972 (Soderblom *et al.* 1973). The first measurement of the polar cap border is performed on November 20 ($L_S = 20^\circ$), when it is located at 62° . At the end of the period of observation ($L_S = 70^\circ$) the border is located around $75-70^\circ$ in latitude. Two distinct phases are apparent on the regression curve: first a linear period from $L_S = 20^\circ$ to 55° , then a standstill from $L_S = 55^\circ$ to 70° at latitude $68-72^\circ$, at least in the $135-300^\circ$ longitude range. This pause in the polar cap retreat corresponds to the approach of aphelion and the subsequent decrease in solar illumination (“aphelic chill”). This behavior is consistent with HST observations, although the time resolution of HST observations is too low to evidence the plateau in the regression curve. Troiani *et al.* 1996 have mentioned a slight regrowth of the cap between 65° and 72° from analyses of ALPO’s telescopic observations. The uncertainty on the Pic-du-Midi images is too large to confirm this. For example, the cap edge seems located at lower latitude on February 22 (longitudes $320-80^\circ$ in Fig. 10), but examination of the images suggests that this larger apparent extension is actually an artifact due to polar clouds (this is the night when the ECB reaches maximum development in the data set).

Conclusion

Several thousands images were acquired on the 1-m telescope during this opposition. After selection, the image quality is extremely good, with spatial resolution reaching 150 km at disk center, and signal to noise ratio on the order of 300 at opposition. Here is a summary of image analysis:

- One of the most striking difference with the 1988 opposition is the darkening of the northernmost part of Terra Cimmeria at longitude 220° and latitude -10° (in the vicinity of Herschel crater).
- The only significant surface variations during the period are observed in the Cerberus area, which brightened at the end of winter, likely in relation with the seasonal migration of bright materials from the adjacent areas.
- A dark collar (the “Lowell band”) developed inside the polar cap between latitudes 78° and 85° . This feature was present as early as November 20 ($L_S = 20^\circ$), and remained apparent until the end of our observation period on March 13 ($L_S = 70^\circ$). The ring was larger and darker at longitudes 120° - 170° and 250° - 320° , in areas of transverse dunes made of basaltic sand and barchan dunes.
- Low resolution spectra were also acquired through a set of interferential filter at opposition, providing indications of mineralogical composition of surface materials. These spectra are in good general agreement with previous observations at higher spatial resolution, with ferric and pyroxenes absorptions in bright and dark regions respectively. However, a special spectral signature is observed in Propontis I: although dark, this region exhibits the deepest absorption band at $0.90 \mu\text{m}$ ($>7\%$) and no absorption at $0.98 \mu\text{m}$, suggesting the occurrence of crystalline hematite or other iron-oxides. Last, the very deep $0.95 \mu\text{m}$ absorption reported from HST observations of Olympia Planitia in July 1995 is not observed here.
- The whole apparition was very cloudy, but at least two clearings were observed on December 16 and February 6. The north Polar Hood dissipated in early December ($L_S \sim 25^\circ$). Migration of polar clouds to the equator was observed between January 31 and February 6 ($L_S \sim 50^\circ$ - 55°). Then an Encircling Cloud Belt obscured most of the surface from February 22 to 24 at least ($L_S \sim 62^\circ$). Although such cloudy situations have been considered precursor signs for large dust storms, only small local storms were observed during this apparition and the following one.

- The north polar cap regression is similar to that observed by Mariner 9, although several internal rifts developed during early springs, in particular the dark Lowell band and Rima Tenuis. A standstill is observed in the polar cap regression curve from $L_S = 55^\circ$ to 70° at latitude $\sim 70^\circ$, at least in the $135\text{-}300^\circ$ longitude range.

HST observations of Mars have numerous advantages over ground-based telescopic observations, in particular significantly better (~ 4 times) spatial resolution, constant image quality and reduction procedure, and the ability to cover the complete longitudinal range on a given day. However, the low frequency of observation does not suffice to monitor quick evolution processes on the surface and the atmosphere. In this regard, ground-based observations on a regular basis from a “small size” telescope located in a good planetary site (with seeing $\sim 0.3''$ at the time scale of 0.1-1 s) still appear as an important complement to higher resolution images. This is particularly true in the frame of the preparation of the on-going Mars exploration program.

Acknowledgments

This paper is dedicated to the memory of Jan Rosenqvist, who initiated this survey of the 1995 apparition of Mars with the Pic-du-Midi 1-m telescope. I am deeply indebted to other members of the observation team, in particular to Jean Lecacheux and François Colas who use and maintain the telescope on a regular basis, and have preserved the efficiency of one of the best planetary instruments in the world. I would also like to thank Patrick Pinet and an anonymous referee for their critical reviews and constructive suggestions. This work has benefited from the support of the French Programme National de Planétologie, which also supports the telescope.

Part of the image processing made use of SIPS (University of Colorado), NASA's IDLastro and IAS's IDLplanets libraries. Other solar System images from the telescope are available at

<http://www.ias.fr/cdp/> (Centre de Données Planétaires at Institut d'Astrophysique Spatiale, Paris)
and <http://www.bdl.fr> (Bureau des Longitudes, Paris).

References:

- Akabane, T., Iwasaki, K., Saito, Y. and Narumi, Y. (1993) Martian late-northern-winter polar hood opacities and non-visibility of a surface cap: 1975 and 1990 observations. *Astron. Astrophys.* **277**, 302-308.
- Antoniadi, E.-M. (1930) *La planète Mars*. Hermann, Paris, 239 pp.
- Bell, J. (1992) Charge-coupled device imaging spectroscopy of Mars 2. Results and implications for Martian ferric mineralogy. *Icarus* **100**, 575-597.
- Bell, J., Thomas, P.C., Wolff, M.J., Lee, S. and James, P.B. (1997a) Mineralogy of the Martian north polar sand sea from 1995 Hubble Space Telescope near-IR observations. In *Lunar and Planetary Science XXVIII*, 87-88. Lunar and Planetary Institute [Abstract].
- Bell, J., Wolff, M.J., James, P.B., Clancy, R.T., Lee, S.W. and Martin, L.Z. (1997b) Mars surface mineralogy from Hubble Space Telescope imaging during 1994-1995: Observations, calibration, and initial results. *J. Geophys. Res.* **102**, 9109-9124.
- Bell, J.F., McCord, T.B. and Lucey, P.G. (1990) Imaging spectroscopy of Mars (0.4-1.1 μm) during the 1988 opposition. *Proc. Lunar Planet. Sci. Conf.* **20**, 479-486.
- Binder, A.B. and Jones, J.C. (1972) Spectrophotometric studies of photometric function, composition, and distribution of the surface materials of Mars. *J. Geophys. Res.* **77**, 3005-3020.
- Cantor, B., Wolff, M., James, P. and Higgs, E. (1998) Regression of Martian North polar cap: 1990-1997 Hubble space telescope observations. *Icarus* **136**, 175-191.
- Capen, C. and Capen, V. (1970) Martian north polar cap, 1962-1968. *Icarus* **13**, 100-108.
- Christensen, P.R., Bandfield, J.L., Clark, R.N., Edgett, K.S., Hamilton, V.E., Hoefen, T., Kieffer, H.H., Kuzmin, R.O., Lane, M.D., Malin, M.C., Morris, R.V., Pearl, J.C., Pearson, R., Roush, T.L., Ruff, S.W. and Smith, M.D. (2000) Detection of crystalline hematite mineralization on Mars by the Thermal Emission Spectrometer: Evidence for near-surface water. *J. Geophys. Res.* , in press.
- Christensen, P.R. and Zurek, R.W. (1984) Martian north polar hazes and surface ice: results from the Viking survey/completion mission. *J. Geophys. Res.* **89**, 4587-4596.

- de Grenier, M. and Pinet, P. (1995) Near-opposition Martian limb-darkening: quantification and implication for visible—near—infrared bidirectional reflectance studies. *Icarus* **115**, 354-368.
- Dollfus, A. (1973) New optical measurements of planetary diameters, IV. Size of the north polar cap of Mars. *Icarus* **18**, 142-155.
- Erard, S., Bibring, J.-P., Mustard, J.F., Forni, O., Head, J.W., Hurtrez, S., Langevin, Y., Pieters, C.M., Rosenqvist, J. and Sotin, C. (1991) Spatial variations in composition of the Valles Marineris and Isidis Planitia regions of Mars derived from the ISM data. *Proc. Lunar Planet. Sci. Conf.* **21**, 437-455.
- Erard, S. and Calvin, W. (1997) New composite spectra of Mars, 0.4-5.7 μm . *Icarus* **130**, 449-460.
- Farmer, C.B., Davies, C.W. and La Porte, D.D. (1976) Mars: Northern summer ice cap-water vapor observations from Viking 2. *Science* **194**, 1339-41.
- Fischbacher, G.E., Martin, L.Z. and Baum, W.A. (1969) *Martian polar caps boundaries*. JPL contract 951547.
- Forget, F. (1997) Mars CO₂ ice polar caps. In *Solar System ices* (B. Schmitt, C. de Bergh and M. Festou, Eds.), pp. 477-510. Kluwer Academic, Toulouse.
- Haberle, R.M. and Jakosky, B.M. (1990) Sublimation and transport of water from the north residual polar cap on Mars. *J. Geophys. Res.* **95**(B2), 1423-1437.
- Iwasaki, K. and Saito, Y. (1979) Behavior of the Martian north polar cap, 1975-1978. *J. Geophys. Res.* **84**, 8311-8316.
- Iwasaki, K. and Saito, Y. (1982) Martian north polar cap 1979-1980. *J. Geophys. Res.* **87**, 10265-10269.
- James, P., Kieffer, H. and Paige, D. (1992) The seasonal cycle of carbon dioxide on Mars. In *Mars* (H. Kieffer, B. Jakosky, C. Snyder and M. Matthews, Eds.), pp. 934-968. University of Arizona Press, Tucson.
- James, P.B. (1979) Recession of Martian north polar cap: 1977-1978 Viking observations. *J. Geophys. Res.* **84**, 8332-8334.
- James, P.B. (1982) Recession of Martian north polar cap: 1979-1980 Viking observations. *Icarus* **52**, 565-569.
- James, P.B., Bell, J., Clancy, R.T., Lee, S.W., Martin, L.J. and Wolff, M.J. (1996a) Global imaging of Mars by Hubble space telescope during the 1995 opposition. *J. Geophys. Res.* **101**, 18883-18890.
- James, P.B., Clancy, R.T., Lee, S.W., Martin, L.J. and Bell, J. (1996b) Seasonal recession of Martian south polar cap: 1992 HST observations. *Icarus* **123**, 87-100.
- James, P.B., Clancy, R.T., Lee, S.W., Martin, L.J., Singer, R.B., E., S., R.A., K. and R.W., Z. (1994) Monitoring Mars with the Hubble Space Telescope: 1990-1991 observations. *Icarus* **109**, 79-101.

- James, P.B., Pierce, M. and Martin, L.J. (1987) Martian north polar cap and circumpolar clouds: 1975-1980 telescopic observations. *Icarus* **71**, 306-312.
- Kieffer, H.H., Chase, S.C., Martin, T.Z., Miner, E.D. and Palluconi, F.D. (1976) Martian north polar summer temperatures: dirty water ice. *Science* **194**, 1341-44.
- Lane, M., Morris, R.V. and Christensen, P.R. (1999) An extensive deposit of crystalline hematite in Terra Meridiani, Mars. In *Lunar and Planetary Science XXX*, abstract #1427. Lunar and Planetary Institute [Abstract].
- Lecacheux, J., Drossart, P., Buil, C., Laques, P., Thouvenot, E. and Guérin, P. (1991) CCD images of Mars with the 1 m reflector atop Pic-du-Midi. *Planet. Space Sci.* **39**, 273-279.
- Martin, L. and Zurek, R. (1993) An analysis of the history of dust activity on Mars. *J. Geophys. Res.* **98**, 3221-3246.
- Martin, P., Pinet, P., Bacon, R., Rousset, A. and Bellagh, F. (1996) Martian surface mineralogy from 0.8 to 1.05 μm TIGER spectro-imagery measurements in Terra Sirenum and Tharsis Montes formation. *Planet. Space Sci.* **44**, 859-888.
- McCord, T.B. and Westphal, J.A. (1971) Mars: Narrow-band photometry, from 0.3 to 2.5 microns, of surface regions during the 1969 apparition. *Astrophys. J.* **168**, 141-153.
- McEwen, A.S. (1991) Photometric functions for photoclinometry and other applications. *Icarus* **92**, 298-311.
- Merényi, E., Edgett, K. and Singer, R. (1996) Deucalionis Regio, Mars: evidence for a new type of immobile weathered soil unit. *Icarus* **124**, 196-307.
- Murchie, S., Merenyi, E., Singer, R. and Kirkland, L. (1996) Visible-NIR spectroscopic evidence for the composition of low-albedo altered soils on Mars. In *Lunar and Planetary Science XXVII*, 919-920. Lunar and Planetary Institute, Houston. [Abstract].
- Paige, D.A., Bachman, J.E. and Keegan, K.D. (1994) Thermal and albedo mapping of the polar regions of Mars using Viking thermal mapper observations, 1. North polar regions. *J. Geophys. Res.* **99**, 25,959-25,991.
- Parker, D.C. and Beish, J.D. (1995) Telescopic observations of Mars: 1994-95 apparition. In Mars telescopic observations LPI [Abstract].
- Pinet, P. and Chevrel, S. (1990) Spectral identification of geological units on the surface of Mars related to the presence of silicates from Earth-based Near-infrared telescopic charge-coupled device imaging. *J. Geophys. Res.* **95**, 14435-14446.

- Soderblom, L.A., Malin, M.C., Cutts, J.A. and Murray, B.C. (1973) Mariner 9 observations of the surface of Mars in the north polar region. *J. Geophys. Res.* **78**, 4197-4210.
- Troiani, D.M., Parker, D.C. and Hernandez, C.E. (1996) The 1994-95 aphelic apparition of Mars. *Strolling Astronon. JALPO* **39**, 1-15.
- Tsoar, H., Greeley, R. and Perterfreund, A. (1979) Mars: the north polar sand sea and related wind patterns. *J. Geophys. Res.* **84**, 8167-8180.
- Warell, J. (1996) Structure of the Martian north polar cap and vernal hood system at Ls 61°-66° of the 1995 apparition. *Earth, Moon, Planets* **74**, 93-107.
- Wolff, M.J., Lee, S.W., Clancy, R.T., Martin, L.J., Bell, J.F. and James, P.B. (1997) 1995 observations of Martian dust storms using the Hubble Space Telescope. *J. Geophys. Res.* **101-2**, 1679-1692.

Figure 1: Selected images acquired in I filter at different solar longitudes. Images are rotated so that the celestial north is on top, and an unsharp mask is applied to enhance local contrasts. Notice the recession of the polar cap, the presence of the dark collar inside the cap, and the variation in the Cerberus area; (a) Elysium hemisphere, images acquired on November 20th, January 31st, February 6th, and March 11th; (b) Sinus Sabeus hemisphere, images acquired on October 2nd, December 16th, and February 22nd. The first image of this series was acquired with a different, lower quality, camera and exhibits a strong horizontal pattern before rotation.

Figure 2: Cylindrical map in I filter, showing surface details near opposition. This map is a composite of images acquired on January 31st (335° - 180° longitude), February 6th (180° - 90°) and February 22nd (90° - 335°). Images are slightly undersampled, processed with an unsharp mask, and corrected for limb darkening before projection. The dynamic range is scaled by continuity, so that contrasts are only indicative.

Figure 3: Evolution of the Cerberus region during the apparition. Although contrast is reduced in the first image, this region appears as a continuous dark feature (November 20). On February 6, it is reduced to three discrete dark spots. Decreasing intensity on the right side of the November image is due to limb darkening.

Figure 4: Composite polar maps in I filter. The mosaics are more or less complete in longitude, depending on observing conditions. Images are (from top to bottom and left to right) from December 12, January 31, February 06 and February 22. The projection is a Lambert one centered at the pole, preserving projected areas. Notice the recession of the polar cap and the development of the Lowell band. Mosaic mismatches are due to limb clouds and limitations of Minnaert's model at large angles.

Figure 5: Spectral ratio of the interferential filters images showed in polar-Lambert projection (down to the Equator), with Minnaert correction applied. The wiggles results from round-off

errors during pixel resampling. (a) Ratio of $0.73\ \mu\text{m}$ to $0.58\ \mu\text{m}$ intensities; the footprints of the spectra in Fig. 6 are shown in white. (b) Band depth at $0.90\ \mu\text{m}$ (see text).

Figure 6: Selected spectra reconstructed from images acquired through the interferential filters on February 6th, and corrected from limb darkening with a Minnaert function. Spectra are averaged over 20 to 40 pixels, in areas shown in Fig. 5. The signal to noise ratio is about 500. The error bars represent the maximum uncertainty related to the Minnaert exponent, and are therefore correlated at different wavelengths. Spectra are scaled to radiance factor using a terrestrial-orbital composite spectrum from Erard and Calvin 1997. Typical spectra of bright regions (Ascræus + Ophir Planum, see text) and dark regions (Margaritifer Terra at 32°W and 17°S) are given for comparison. Notice the unusual absorption at $0.90\ \mu\text{m}$ on the Propontis I spectrum.

Figure 7: Selected images in B filter showing atmospheric activity (a) December 16 under clear atmosphere. Notice the bright limb haze, polar clouds and the structure inside the cap; (b) February 6, clear atmosphere. Bright orographic clouds are present on the Tharsis volcanoes and Alba Patera, but surface contrast is very large; (c) February 22, when the Equatorial Cloud Belt has developed. Surface markings are barely visible, the more cloudy regions are as bright as the polar cap.

Figure 8: Composite cylindrical maps in B filter, with selected altimetric contours superimposed (from the Viking DTM): (a) January 31, under clear atmosphere (the cap is saturated to increase contrast at lower latitudes) and (b) February 22, when the Equatorial Cloud Belt is fully developed (maximum intensity is observed over Tharsis, so the scaling is different from the other map — see Fig. 7b and 7c).

Figure 9: Regression curve of the north polar cap. Measurements are performed at the central meridian of I and R images, and compared with average HST measurements of the same opposition by Cantor *et al.* 1998 (dashed line). Notice the plateau in the regression rate between

55° and 70°, corresponding to the aphelic chill (aphelion is at 71°). The large dispersion at $L_S = 62.2^\circ$ corresponds to the maximum development of the encircling cloud belt.

Figure 10: Location of the cap edge as a function of longitude and areocentric longitude of the Sun L_S . Measurements are derived from I and R images, $\pm 40^\circ$ apart from the central meridian.

Night	Angular size (")	L _S (°)	Phase angle (°)
Oct 01, 1994	5.94	355.55	37.4
Oct 02	5.97	356.06	37.4
Nov 19	7.84	19.45	37.9
Nov 20	7.89	19.92	37.9
Nov 21	7.95	20.40	37.8
Dec 06	8.91	27.38	35.9
Dec 08	9.05	28.30	35.6
Dec 10	9.20	29.22	35.2
Dec 11	9.28	29.68	35.0
Dec 12	9.35	30.14	34.7
Dec 13	9.43	30.60	34.5
Dec 15	9.59	31.52	34.1
Dec 16	9.67	31.97	33.8
Jan 31, 1995	13.56	52.58	10.3
Feb 01, 1995	13.61	53.02	9.5

Night	Angular size (")	L _S (°)	Phase angle (°)
Feb 02	13.65	53.46	8.8
Feb 03	13.69	53.90	8.0
Feb 04	13.73	54.34	7.2
Feb 05	13.76	54.78	6.5
Feb 06	13.79	55.22	5.7
Feb 09	13.85	56.54	3.7
Feb 10	13.86	56.98	3.2
Feb 12	Opposition		
Feb 20	13.70	61.36	7.0
Feb 22	13.62	62.24	8.6
Mar 09	12.57	68.79	19.2
Mar 11	12.40	69.66	20.4
Mar 13, 1995	12.22	70.54	21.6
Mars 14	Aphelion		

Table 1: observational parameters for nights with good observational conditions.

Filter name in text	Center wavelength (Å)	Width at half-height (Å)	Typical S/N ratio
Broad band			
B	4400	1500	300
V	5500	1000	300
R	6750	2000	300
RG 695	8500	2500	300
I	8750	1500	300
Pinet and Chevrel's filters			
0.40	4014	94	150
0.73	7300	91	300
0.90	9000	90	300
0.98	9800	85	200
1.02	10203	87	200
Other interferential filters			
0.51	5142	80	300
0.58	5830	50	300

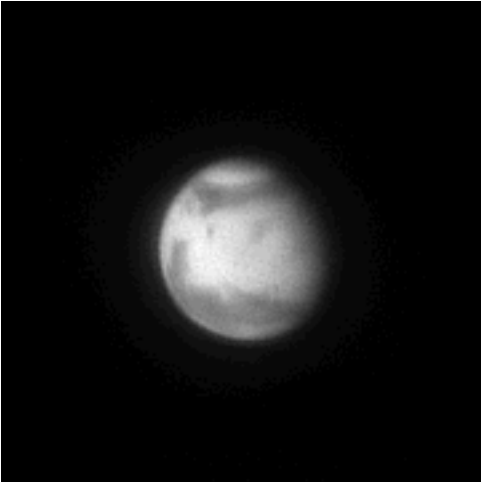
Table 2: characteristics of the filters used in this paper. Pinet and Chevrel's filters were made to measure. The actual spectral range is also limited by the CCD response function (0.4-1.0 μm). Signal to noise ratio is estimated over medium albedo regions near opposition.

Date / Image #	Central longitude	$k \pm \Delta k$	1 - r	Number of points
31 / 01 /95 27	190.6°			
157	271.0°	0.69 ± 0.03	9.1 %	2080
06 / 02 /95 30	113.1°			
140	220.9°	0.69 ± 0.02	9.5 %	1600
170	243.3°	0.65 ± 0.06	6.0 %	5300
22 / 02 /95 47	341.0°			
79	20.1°	0.66 ± 0.03	6.7 %	4320
196	76.9°	0.63 ± 0.03	7.3 %	3360

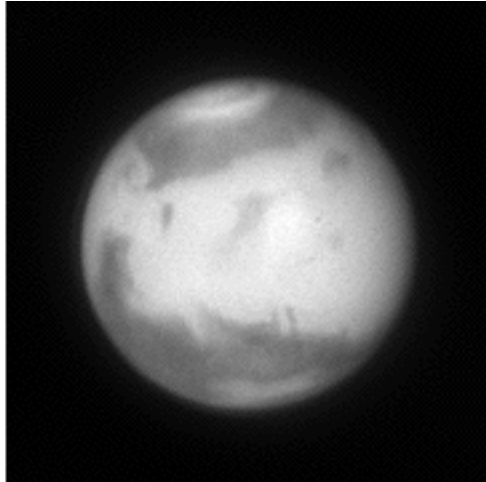
Table 3: Minnaert exponents in I filter, retrieved from images used in the cylindrical map on Fig. 2. The optimal exponent is the value that minimizes the residual dispersion in the image overlap (1 - r).

Date / Image #	Central longitude	$k \pm \Delta k$	1 - r	Number of points
31 / 01 /95 6	191.4°			
34	244.1°	0.57 ± 0.03	10.0 %	3599
45	269.8°	0.56 ± 0.05	3.2 %	5039
22 / 02 /95 12	18.5°			
22	33.2°	0.53 ± 0.05	5.1 %	5600
30	77.4°	0.49 ± 0.03	10.5 %	4080

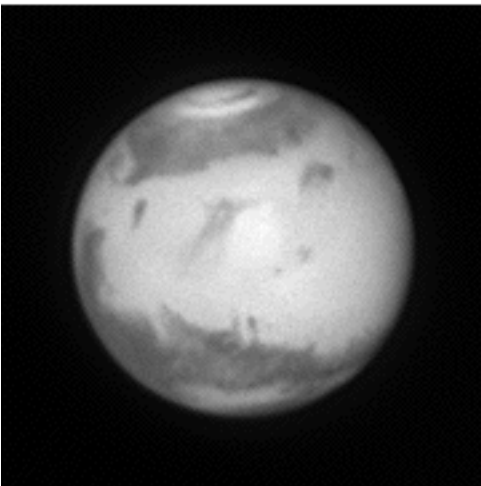
Table 4: Same as Table 3 for B images used in maps on Fig. 8. The very low values computed on February 22 correspond to high atmospheric opacity.



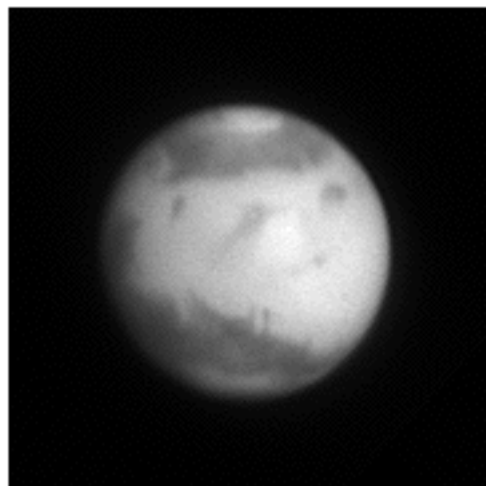
$L_s = 19.9^\circ$



$L_s = 52.6^\circ$



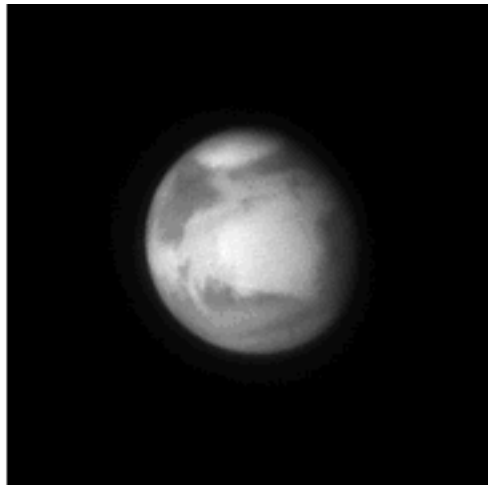
$L_s = 55.2^\circ$



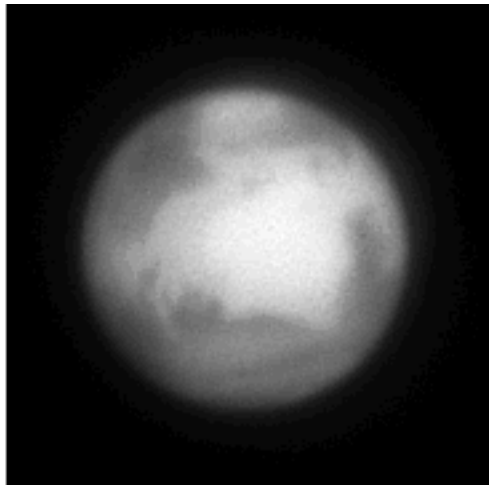
$L_s = 69.7^\circ$



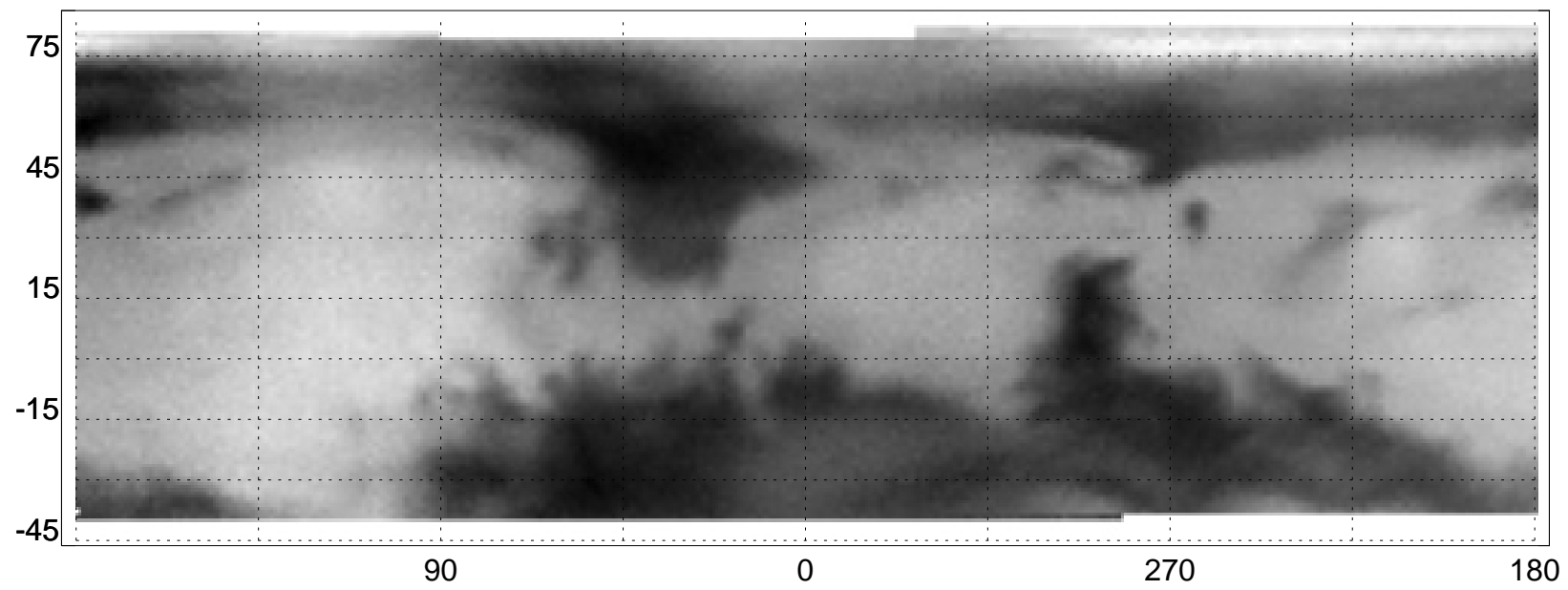
$L_s = 356.1^\circ$

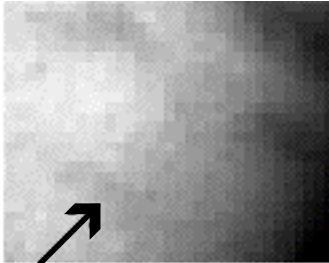


$L_s = 32.0^\circ$

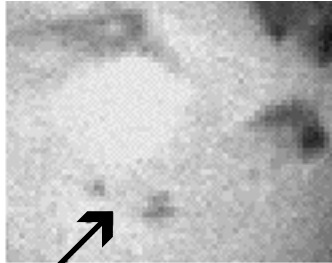


$L_s = 62.2^\circ$

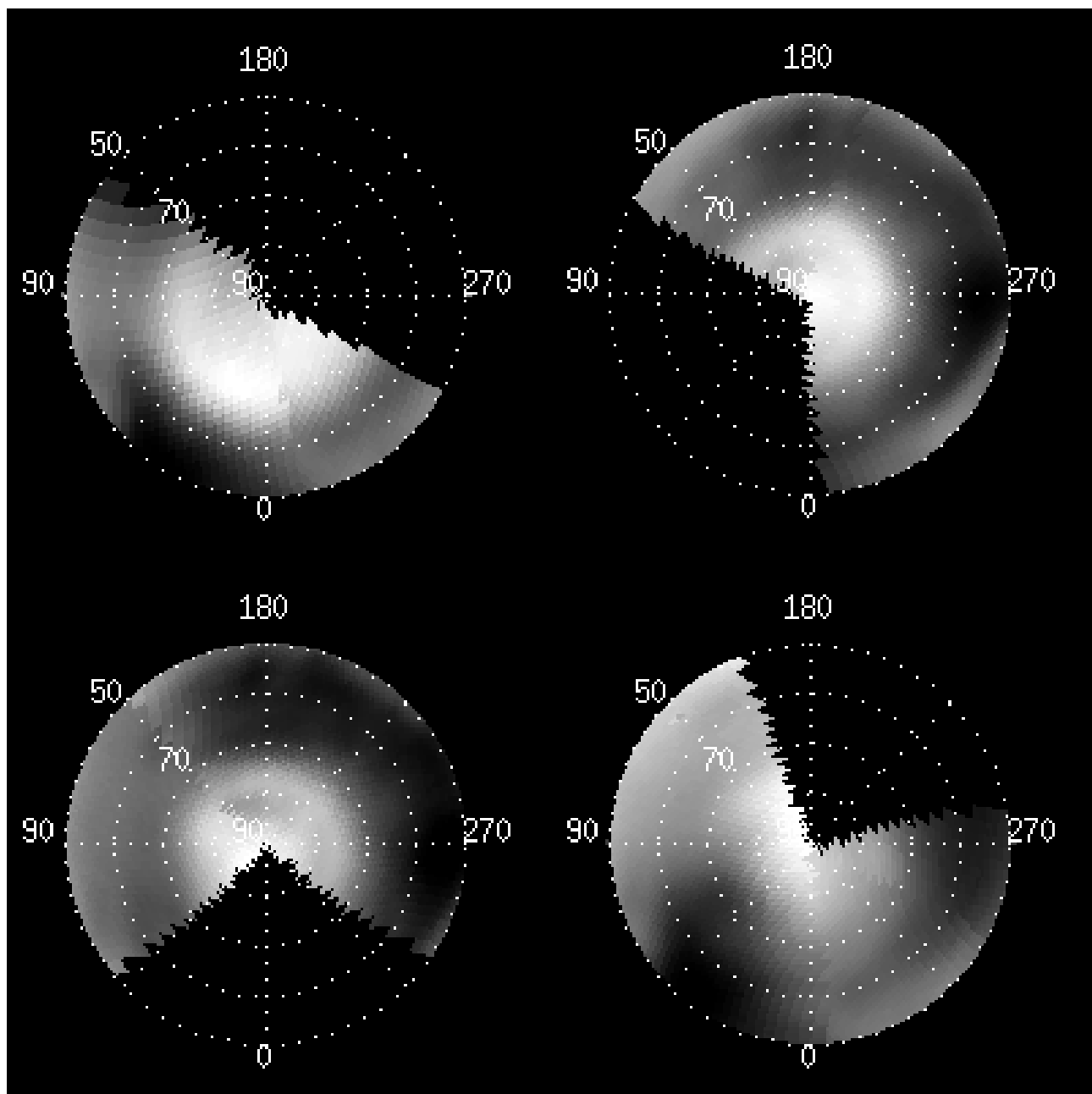


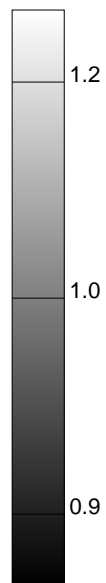
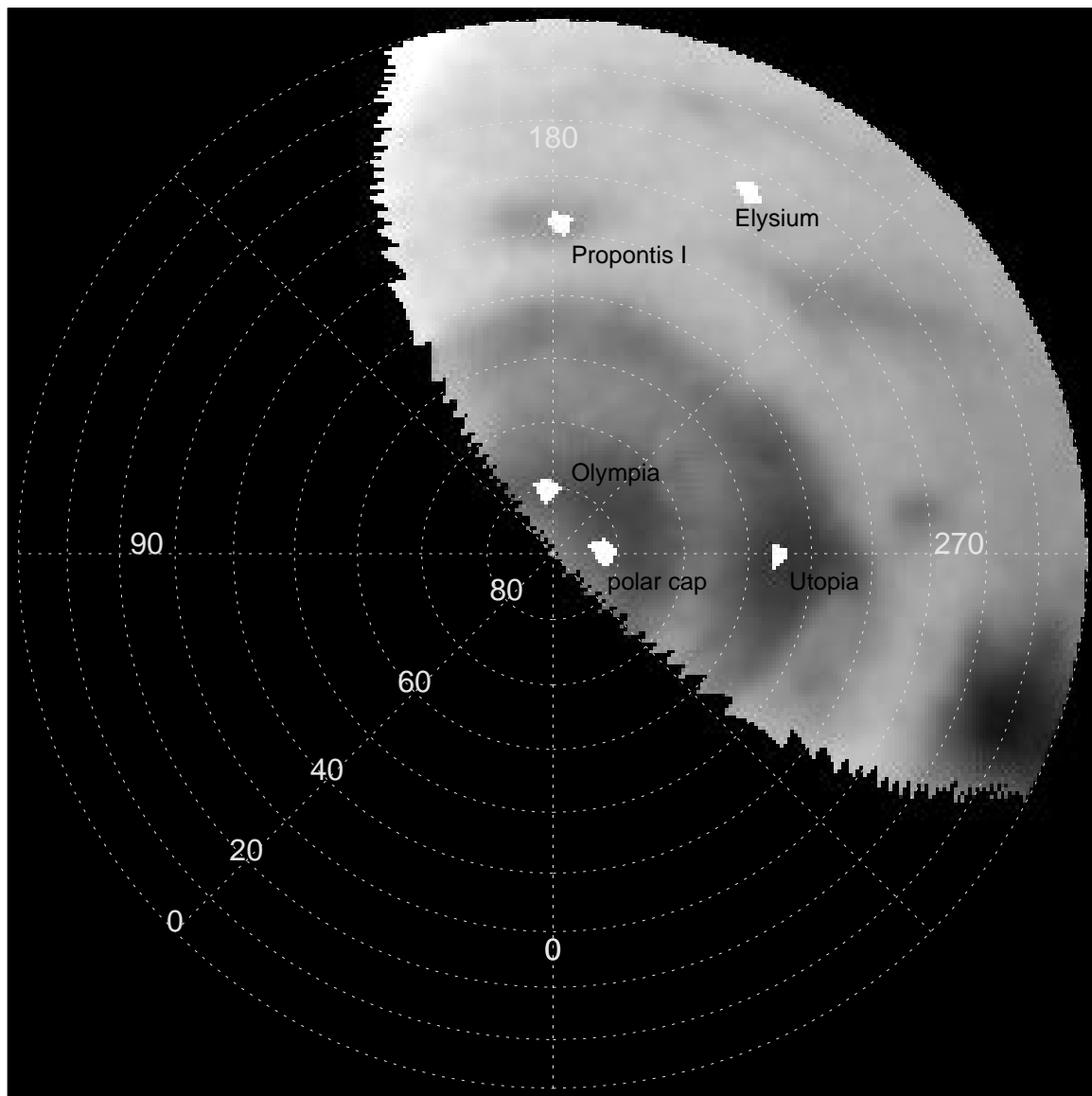


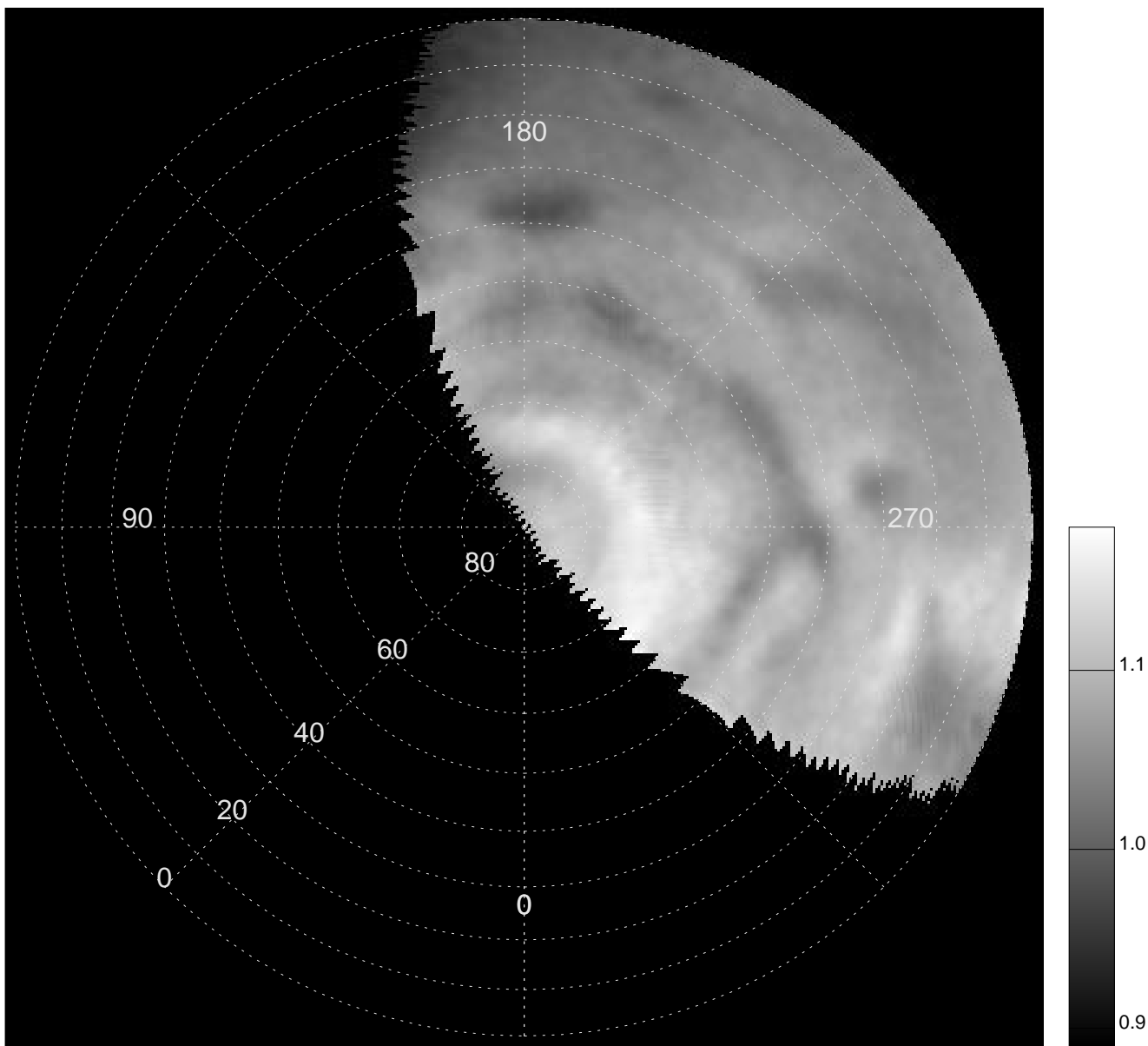
November 19th

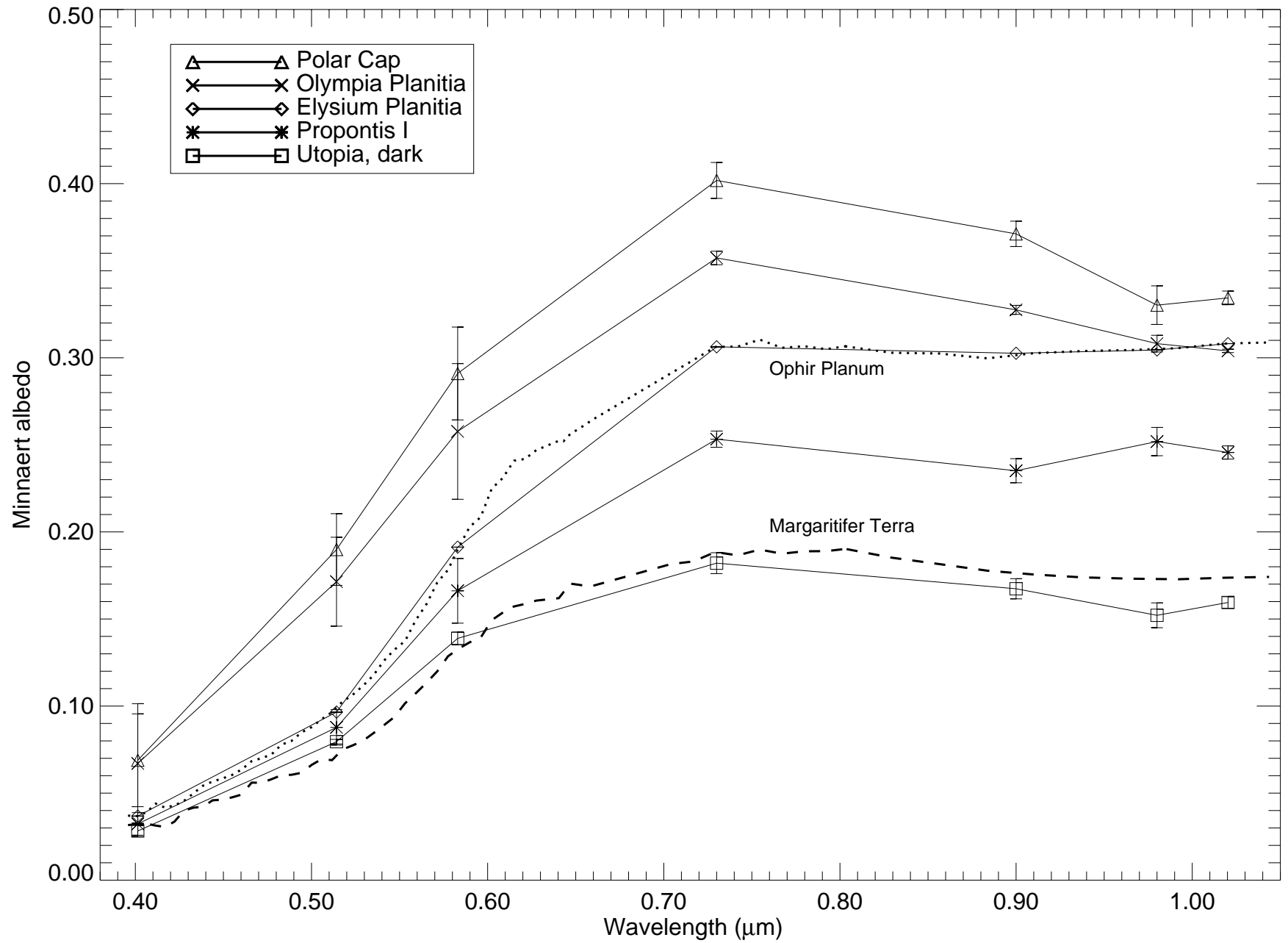


February 6th

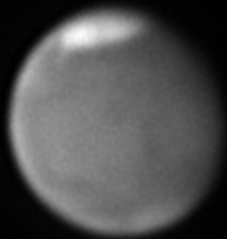




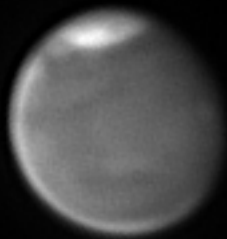




16 dec 1994

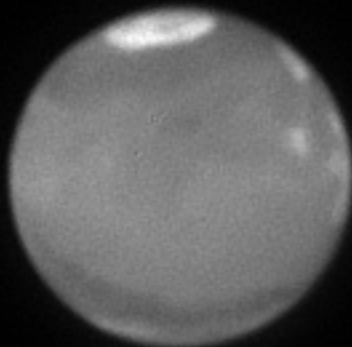


1h 36'52".92

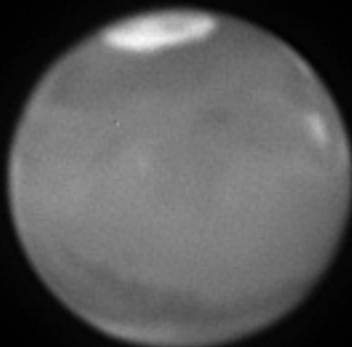


3h 44'53".60

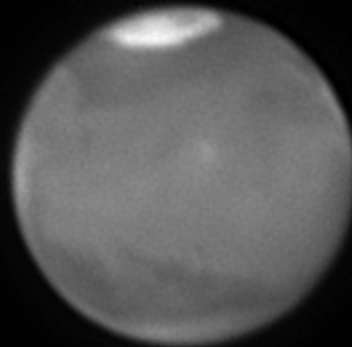
6 Feb 1995



0h 52' 12".40

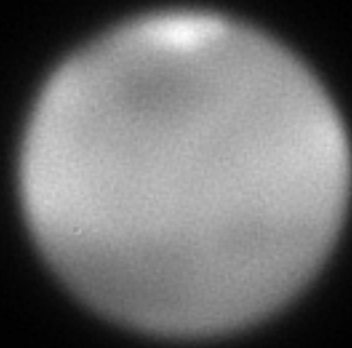


1h 50' 55".21

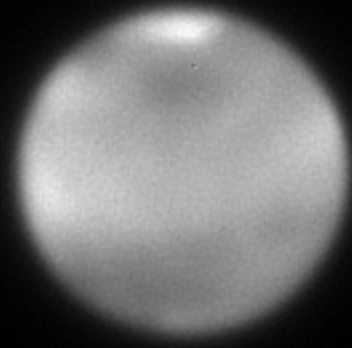


3h 27' 16".77

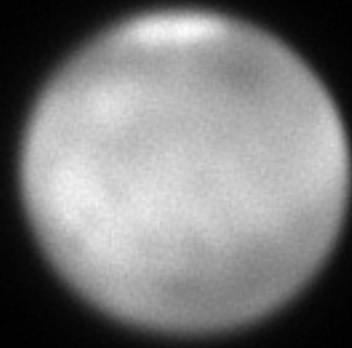
22 feb 1995



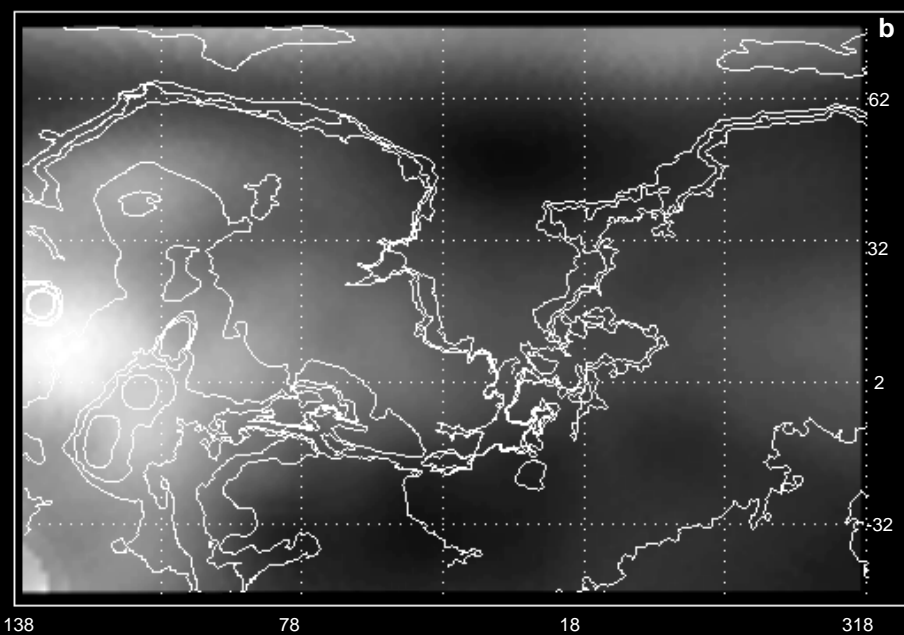
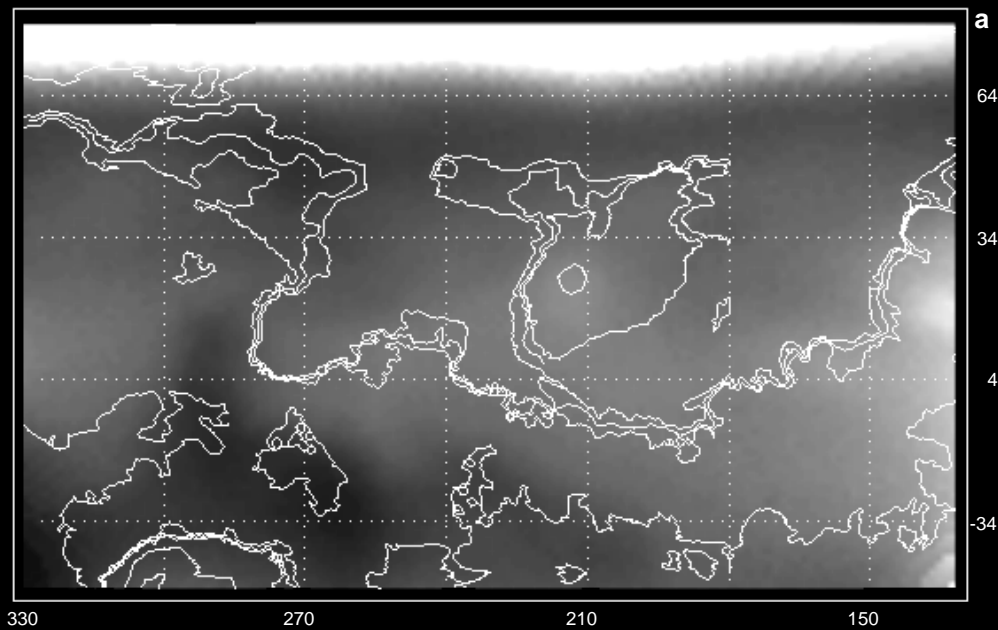
22h 58' 11".20

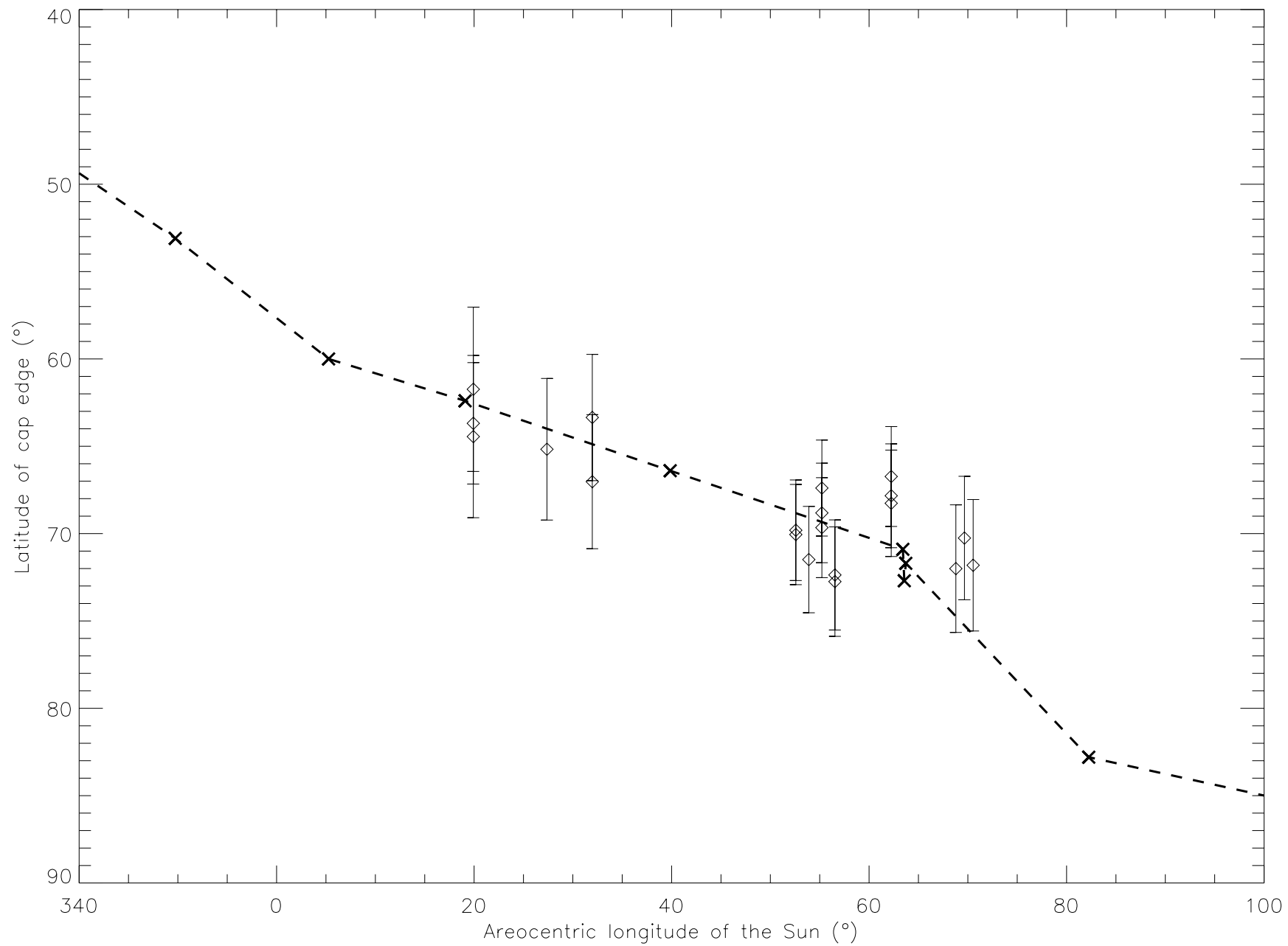


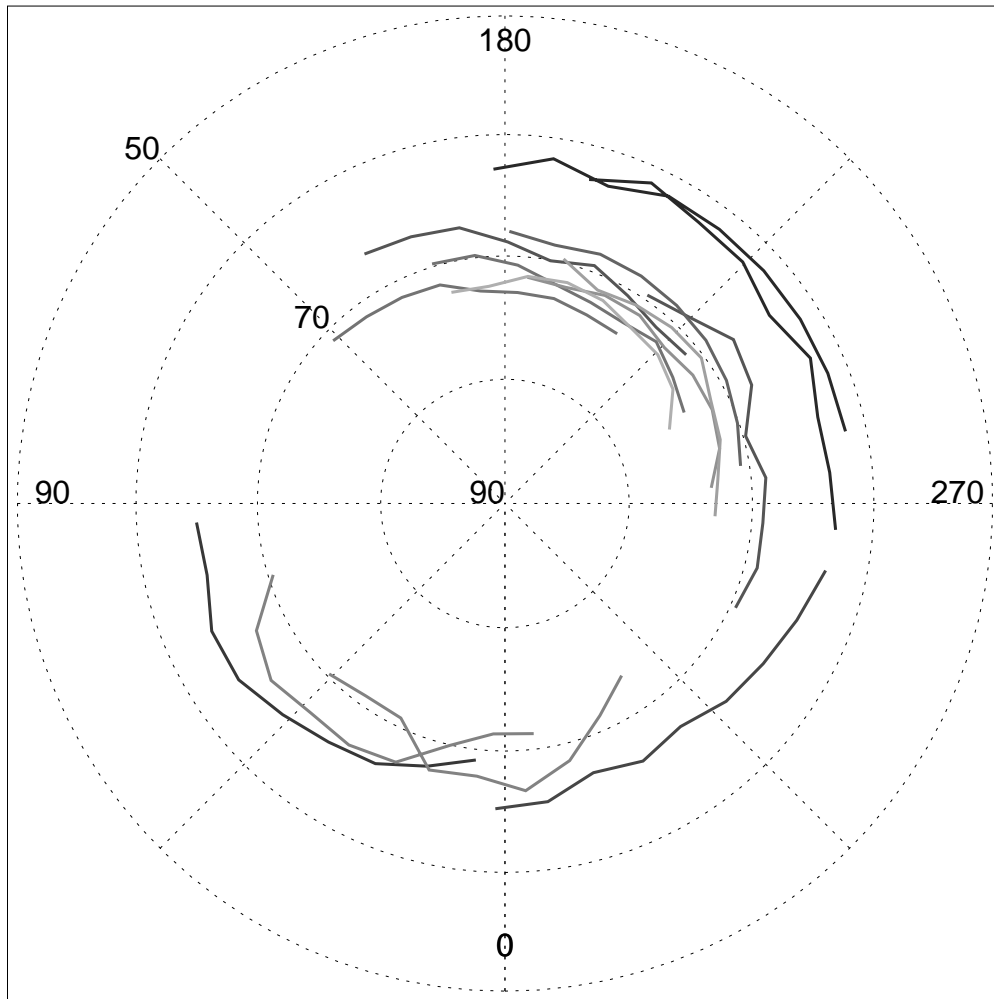
23h 58' 11".95



2h 09' 03".30







Solar longitude (°):

—	19.92
—	27.38
—	31.97
—	52.58
—	55.22
—	56.54
—	62.24
—	68.79
—	69.66
—	70.54